nature photonics

SUPPLEMENTARY INFORMATION

https://doi.org/10.1038/s41566-017-0089-9

In the format provided by the authors and unedited.

Large optical nonlinearity of nanoantennas coupled to an epsilon-near-zero material

M. Zahirul Alam[1], Sebastian A. Schulz[1,2,3], Jeremy Upham[1], Israel De Leon[4*] and Robert W. Boyd[1,5]

[1]Department of Physics, University of Ottawa, Ottawa, ON, Canada. [2]Centre for Advanced Photonics and Process Analysis, Cork Institute of Technology, Cork, Ireland. [3]Tyndall National Institute, Cork, Ireland. [4]School of Engineering and Sciences, Tecnologico de Monterrey, Monterrey, NL, Mexico. [5]Institute of Optics and Department of Physics and Astronomy, University of Rochester, Rochester, NY, USA. *e-mail: ideleon@itesm.mx

Linear response of ITO

We measured the permittivity of the 23 nm ITO using ellipsometry (Fig.S1). For the entire spectral range the following Drude-Loretz model can quantify the permittivity:

$$\varepsilon = \varepsilon_\infty + \frac{(\varepsilon_s - \varepsilon_\infty)\omega_t^2}{\omega_t^2 - \omega^2 - i\Gamma_0\omega} - \frac{\omega_p^2}{\omega^2 + i\Gamma_d\omega}. \tag{1}$$

We use the following values for the parameters. $\varepsilon_\infty = 3.1178$, $\varepsilon_s = 3.8466980$, $\omega_t = 7.42969 \times 10^{15}$ rad/sec, $\omega_p = 2.6594 \times 10^{15}$ rad/sec, $\Gamma_0 = 0.534217 \times 10^{15}$ rad/sec, $\Gamma_d = 0.231806 \times 10^{15}$ rad/sec.

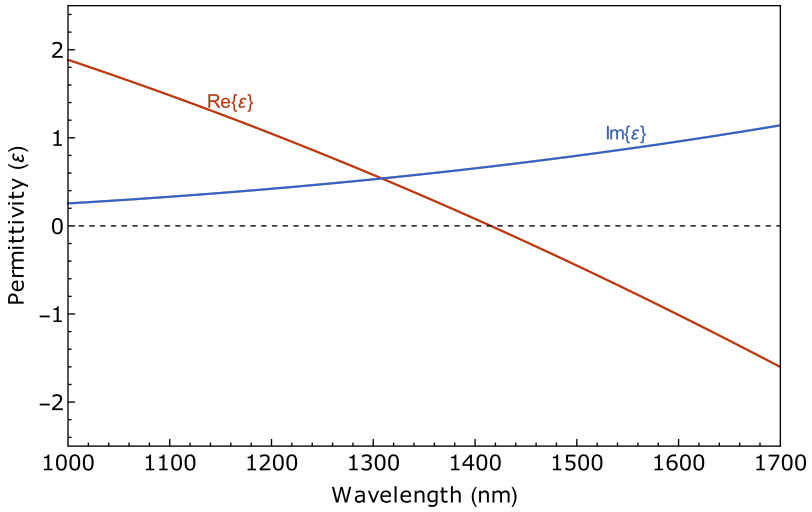

Figure S1. Permittivity of ITO: The real part of permittivity of the low conductivity ITO crosses zero at 1420 nm.

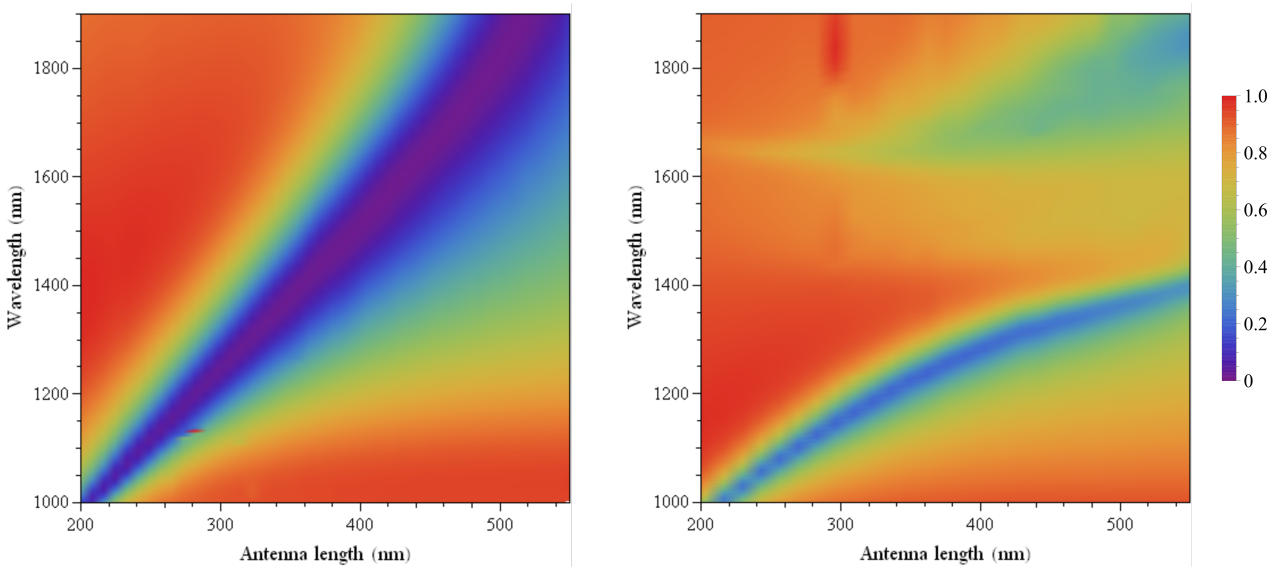

Figure S2. Strong coupling: Length dependent variation in the transmittance of gold dipole antenna on glass in the absence of an ITO layer (left panel) and with an ITO layer between the antenna and the substrate (right panel).

Linear response of the coupled system

A thin ENZ layer supports a bulk plasma mode with wavevector-dependent radiative and nonradiative properties at the zero permittivity wavelength. This mode has been theoratically and experimentally investigated in a number of papers.[1,2] When a

dipole antenna with resonance near the bulk plasma mode is placed on the ITO layer, the antenna mode and the bulk plasma mode interacts. This interaction results in strong coupling induced splitting of the antenna resonance. Fig. S2 shows an anti-crossing in the coupled structure which is a signature that antenna-ITO is in strong coupling regime. This artificial polariton splitting ($\sim \lambda/4$) is one of the largest observed in metamaterials.[3–5] The shape and the magnitude of the resonance dips of the ITO-antenna coupled structure depend on the coupling strength and the material parameters. The spectral width of the resonance of the coupled system at the shorter wavelength is narrower than that of antenna only.

Electronic dispersion relation in ITO

ITO has a non-parabolic conduction band.[6] Following Kane's model[7,8] of semiconductor we can write the energy-wavevector (E, k) dispersion relation for a conduction band electron of ITO as

$$\frac{\hbar^2 k^2}{2m} = E + CE^2, \tag{2}$$

where $C = 0.4191$ eV^{-1} is the non-parabolicity parameter and we have used the value reported by Liu et. al.[6] $m = 0.4m_e$ is the effective mass of the electrons. From the above relation we find

$$k = \sqrt{2mE(1+CE)/\hbar^2}, \tag{3}$$

$$dk = \sqrt{\frac{2m}{\hbar^2}}\frac{1+2CE}{2\sqrt{E+CE^2}}dE. \tag{4}$$

The number of states available for a given magnitude of wavevector $|k|$ can be found by constructing a spherical shell of radius $|k|$ and thickness dk. The volume of this spherical shell in the momentum space is $4\pi k^2 dk$. The number of k states within the spherical shell, $g(k)dk$, is

$$g(k)dk = \frac{1}{2^3} \times 2 \times 4\pi k^2 \frac{V}{\pi^3} dk. \tag{5}$$

The factor 2 is the spin degeneracy factor of electrons. The factor $1/2^3$ is to avoid counting indistinguishable wavefunctions differing in signs only. Now by using Eqns. (3) and (4) and by dividing by the volume V, we can find the density of states $g(E)$, defined as the number of electron states in the conduction band per unit volume over an energy range dE,

$$g(E) = \frac{\sqrt{2}}{\pi^2}\left(\frac{m}{\hbar^2}\right)^{\frac{3}{2}} [(1+CE)]^{\frac{1}{2}} (1+2CE) \tag{6}$$

The total number of electrons n can be found by integrating the product of the Fermi-Dirac distribution function (f_{FD}) and the density of states over all energy range

$$n = \int_0^\infty f_{FD}(E, \mu(T_e), T_e) g(E) dE, \tag{7}$$

where $\mu(T_e)$ is the electro-chemical potential which depends on the electron temperature T_e due to the conservation of total electron number in the conduction band. Thus, the electron number conservation requirement results in decreasing value of the chemical potential with increasing electron temperature.

We can write the plasma frequency as[9,10]

$$\omega_p^2(T_e) = \frac{e^2}{3m\varepsilon_0\pi^2} \int_0^\infty dE(1+2CE)^{-1} \left(\frac{2m}{\hbar^2}(E+CE^2)\right)^{\frac{3}{2}} \left(-\frac{\partial f_{FD}(E, \mu(T_e), T_e)}{\partial E}\right). \tag{8}$$

The expression $\left(-\frac{\partial f_{FD}}{\partial E}\right)$ is a measure of the strength of the thermal broadening of the electronic distribution around the Fermi level. For electrons in a room temperature solid the thermal broadening function is narrow and is zero beyond a few $k_B T$ from the Fermi level. However, an elevated electron temperature leads to the broadening of this function due to a strong modification of the Fermi-Dirac distribution. The modification of the Fermi-Dirac distribution is much stronger in ITO than a noble metal due to the lower heat capacity constant of the free electrons of ITO. This results in an electron-temperature-dependent plasma frequency of ITO due to the temperature dependence of the electro-chemical potential (the effective mass of the electrons) as required by Eq.(7). For a given electronic temperature we find the chemical potential from Eqn. (7), and use Eqn. (8) to find the plasma frequency of ITO which we insert into the Drude-Lorentz model of ITO to calculate the permittivity of ITO at an elevated electron temperature. For a parabolic band ($C = 0$) the above expression reduces to the well known expression of the plasma frequency.[10]

Two-temperature model

The free-electron dynamics in ITO are metal-like and can be described by the Drude model. The third-order self-focusing nonlinearity of ITO in the ENZ regime is dominated by the response of the free-electrons. To describe this nonlinear mechanism, we use a phenomenological two-temperature model.[11–13] The nonlinear process due to the hot-electron dynamics has a finite response time and the maximum response is delayed with respect to the peak of the laser excitation. In noble metals the total relaxation time of the hot electrons is a few picoseconds and is limited by the electron-phonon interaction time. However the response of the ITO thin film deviates from that of the metal in three important ways: i) unlike noble metals, ITO has no interband transition resonance in the visible or infrared range of the optical spectrum; ii) the free-electron density in ITO is almost two orders of magnitude smaller than that of noble metals such as gold, resulting in much smaller electron heat capacity and larger change in the electron temperature if all other parameters are held constant; and iii) owing to a relatively smaller free-electron density, the Fermi level is quite low in the conduction band (~ 1 eV for ITO). Due to the last property, infrared radiation at ENZ wavelengths can excite even the lowest-energy conduction band electrons (in contrast, the Fermi level of gold is ~ 6.42 eV and IR light only excite only those electrons that sit near the Fermi level).

According to the delayed two-temperature model, after the laser pulse is absorbed, the generated hot electrons acquire a non-thermal energy distribution and act as a delayed source of energy. The overall dynamics of the conduction band electrons can be described by the following system of phenomenological coupled differential equations:[13]

$$\begin{aligned} C_e\frac{\partial T_e(t)}{\partial t} &= -g_{ep}(T_e(t)-T_l(t))+\frac{N_{th}(t)}{2\tau_{ee}(t)}, \\ C_l\frac{\partial T_l}{\partial t} &= g_{ep}(T_e(t)-T_l(t))+\frac{N_{th}}{\tau_{ep}(t)}, \\ \frac{\partial N(t)}{\partial t} &= -\frac{N(t)}{2\tau_{ee}(t)}-\frac{N(t)}{\tau_{ep}(t)}+P, \end{aligned} \tag{9}$$

Here, N is the non-thermal energy density stored in the excited electrons, g_{ep} is the electron-phonon coupling coefficient, T_e (T_l) is the free-electron (lattice) temperature, C_e (C_l) is the heat capacity of the electrons (lattice), τ_{ee} (τ_{ep}) is the electron-electron (electron-phonon) relaxation time, and P is the time dependent absorbed power density (i.e., rate of energy density absorbed in the material). We have ignored thermal diffusion processes in Eq. (9). In the transverse dimension the beam size greatly exceeds the electrons thermal diffusion length and hence we also ignore the transverse dependence. We have also ignored the thermal diffusion in the longitudinal direction by assuming constant absorbed energy density due to small thickness of the ITO film.

Next we estimate the different parameters for ITO that appear in Eq. (9). We calculate the electron heat capacity C_e by using[14]

$$C_e(T_e)=\int Eg(E)\frac{\partial f_{FD}(\mu(T_e),T_e)}{\partial T_e}dE \tag{10}$$

We take the lattice heat capacity $C_l = 2.54\times10^6$ Jm^{-3}K to be a constant due to relatively small change in the lattice temperature.[15]

The electron-electron scattering rate ($\Gamma_{ee}=1/\tau_{ee}$) determines the time duration electrons require to reach to thermal equilibrium with each other. We use the following relation to estimate the temperature dependent electron-electron scattering rate[16]

$$\Gamma_{ee}=\frac{\omega^2}{4\pi^2\omega_p(T_e)}\left[1+\left(\frac{2\pi k_B T_e}{\hbar\omega}\right)^2\right] \tag{11}$$

The electron-phonon scattering rate (Γ_{eph}) depends on the lattice temperature and the Debye temperature of the lattice ($\Theta_D = 900K$)

$$\Gamma_{eph}=\Gamma_0\left[\frac{2}{5}+\frac{4T_L^5}{\Theta_D^5}\int_0^{\theta_D/T_l}\frac{z^4}{e^z-1}dz\right]. \tag{12}$$

The electron-phonon coupling coefficient (g_{ep}) determines the rate of the energy exchange between the excited hot electrons and the vibrational modes of the lattice. Due to the strong modification of the conduction band electron distribution, even the electrons with initial energy much below the Fermi level take part in this energy exchange process. Hence we estimate the electron-phonon coupling coefficient using a relation which includes the density of states of the conduction band[14]

$$g_{ep}=\frac{\pi k_B}{\hbar g(E_F)}\lambda_{ep}<(\hbar\omega_{ph})^2>\int g^2(E)\frac{-\partial f_{FD}}{\partial E}dE, \tag{13}$$

where λ_{ep} is the electron-phonon mass enhancement parameter and the second moment of phonon spectrum $< (\hbar\omega_{ph})^2 >$ is an empirical parameter. We take $\lambda_{ep} < (\hbar\omega_{ph})^2 >= 0.0042\ eV^2$ are a few times smaller than nobel metals such as gold.[14]

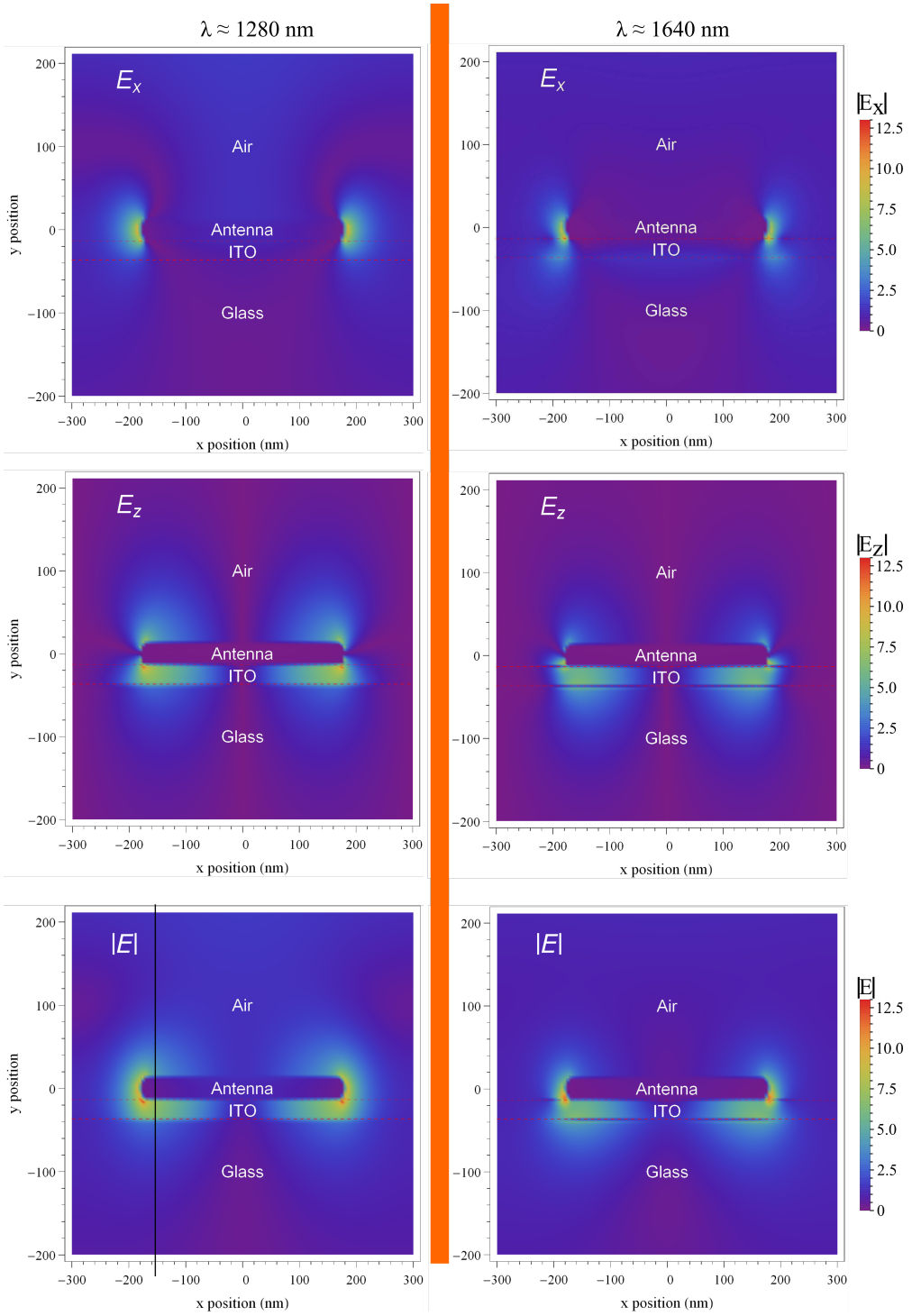

Figure S3. Field distribution: The plots show the field distribution at two resonances ($\lambda \approx 1280$ nm and $\lambda \approx 1640$ nm). The left panel shows the field distribution of the resonance at the short wavelength (the resonace of interest for this report). The right panel shows the field distribution at the resonance located at the long wavelength (we have not investigated the response at this wavelength). The z-components of the electric field profile shows the main difference between the two modes of the coupled structure. The edges of the antennas are rounded with a rounding radius of 7 nm. We plot the wavelength-dependent intensity enhancement along the vertical black line in the next figure.

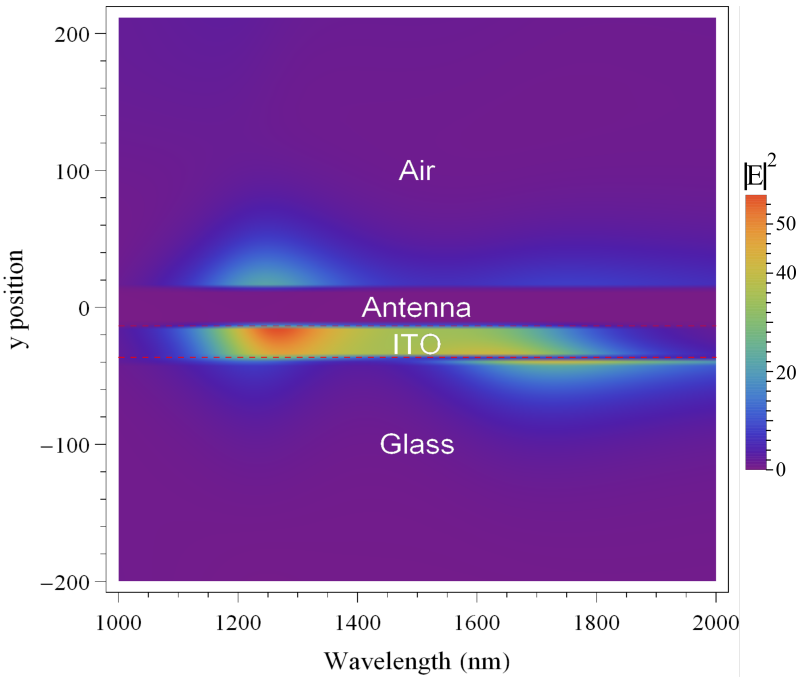

Figure S4. Wavelength-dependent intensity enhancement: Shown inside the ITO layer of the coupled structure, for a fixed x-position – along the vertical black line in Fig. S3 – when excited from air.

Field enhancement and absorption

The antennas placed on the ITO film allow electric field to be concentrated inside the ITO structure resulting in enhancement of the field intensity. Figure S4 shows the calculated intensity enhancement factor, as a function of position and wavelength, sufficiently far from the antenna edge to avoid hotspots. The fabricated dipole antennas differ from the simulated ones due to the fabrication imperfection which results in antenna edges being rounded off. We took this into account in the simulation by rounding the edges (7 nm rounding radius) of the antennas. Furthermore, in our calculation of the two-temperature model we take the calculated intensity enhancement (averaged over the ITO thickness) by considering the electric field enhancement sufficiently far away from the antenna edge (along the vertical black line in the lower left panel of Fig. S3).

The absorption spectrum of the coupled system also differs significantly from the absorption coefficient of the bare ITO (Fig. S5). Due to the stronger interaction of light with the ITO and the loss introduced by the plasmonic antennas, the absorption coefficient is higher close to the resonances of the coupled system (maximum absorption is $\sim 30\%$ within the spectral range of interest in this paper). Thus the antenna array increases the absorbed power density in the ITO film which results in the enhancement of the nonlinear response of the overall system. However, a significant fraction of the power is absorbed by the antennas which can be reduced by using dielectric antennas.

Nonlinear response of ITO

We measured the nonlinear response of the 23-nm-thick ITO sample use a Z-scan technique at normal incidence. The 23-nm-thick ITO film exhibits wavelength dependent positive nonlinear refraction and saturable absorption. The maximum value of n_2 is $\sim 1.5 \times 10^{-3}$ at $\lambda = 1400$ nm with ~ 200 GW/cm^2 incident intensity. Thus ~ 200 GW/cm^2 of incident intensity induces a change of 0.15. It can be explained, to first approximation, due to a 5% red-shift in the plasma frequency. In order to find the nonlinear response of the ITO film, we measured the nonlinear response of the ITO coated substrate (float glass) and the nonlinear response of a similar substrate seperately while keeping the incident intensity constant. We then used the relation $n_{2,\mathrm{ITO}} = (n_{2,\mathrm{ITO-with-substrate}} L_{\mathrm{ITO-with-substrate}} - n_{2,\mathrm{substrate}} L_{\mathrm{substrate}})/L_{\mathrm{ITO}}$ to find the n_2 of the ITO layer. Here, L denotes the thickness.

Refractive index homogenization

The effective linear refractive index of the medium depends on the Q-factor of the resonator and the coupling dynamics between the antennas and the ENZ film. We used the metamaterial homogenization procedure introduced by Smith et al.[17] to calculate the effective refractive index of the hybrid structure. We use the following set of equations to find both the real and the imaginary

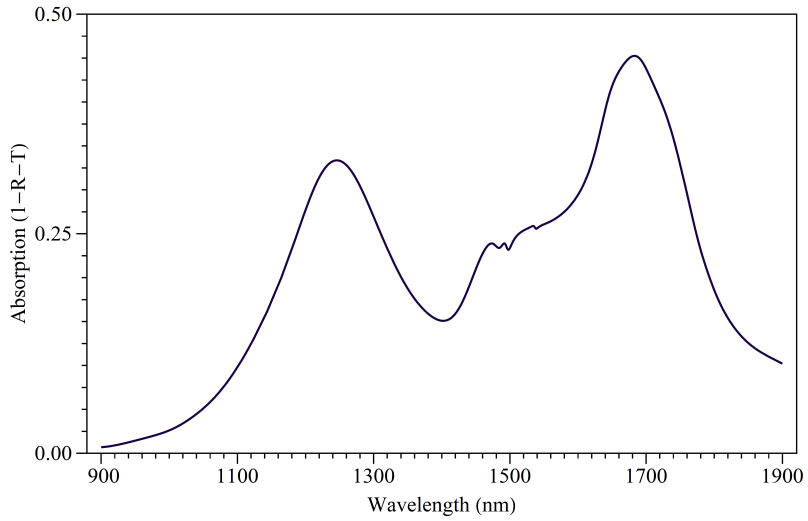

Figure S5. Absorption: Calculated absorption profile by the ITO-antenna coupled structure. The two peaks in the profile - one at a shorter wavelength than the zero-crossing wavelength and one at a larger wavelength - further confirms the strong coupling dynamics between ENZ mode and the antenna mode. Within the spectral range of interest the the theoratical maximum absorption is $\sim 34\%$.

part of the homogenized effective linear refractive index (Figure S7)

$$\begin{aligned} s_{av} &= \sqrt{s_{11}s_{22}} \\ z &= \sqrt{\frac{(1+s_{av}^2-s_{21}^2)}{(1-s_{av})^2-s_{21}^2}} \\ n_{eff} &= \frac{\imath}{2\pi d_{ITO}/\lambda}\log\left[\frac{s_{21}}{1-s_{av}\frac{z-1}{z+1}}\right] \end{aligned} \tag{14}$$

We calculated the plasma-frequency-dependent homogenized refractive index by calculating the s-parameters using a series of FDTD simulations while manually varrying the zero permittivity wavelength of the ITO film. The two-temperature model and the plasma-frequency-dependent homogenized refractive index of the overall system allows us to calculate the nonlinear refractive index of the antenna-ITO coupled system.

Change in plasma frequency and nonlinear index

To first approximation the change in the refractive index of ITO and that of the coupled system can be attributed to the red-shift of the plasma frequency as a function of incident intensity.[9,10,18,19] For example, a 5% change in the plasma frequency ($\Delta\omega_p = 5\%$) leads to a change in the refractive index of the bare ITO layer by ~ 0.16 at $\lambda = 1400$ nm which can be achieved with incident intensity of 100 GW/cm^2. Whereas, for the coupled system a red-shift of the plasma frequency leads to a much larger change in the refractive index. Depending on which spectral side of the resonance is under investigation, the change in the refractive index, Δn, can be either positive or negative. For example, in the coupled system $\Delta\omega_p = 5\%$ leads $\Delta n = -5$ and $\Delta n = 1.16$ at $\lambda = 1280$ nm and $\lambda = 1440$ nm respectively (Fig. S8). However, experimentally we measure $\Delta n_{max} \approx -2.5$ at 1280 nm and $\Delta n_{max} \approx 2.5$ at $\lambda = 1440$ nm. Thus, this simple analysis based on the red-shift of the plasma frequency overestimates the Δn_{max} on- and near- resonance but underestimates the changes far from the resonance. The change in the electronic temperature not only red-shifts the plasma frequency of the ITO but also increases the damping coefficent, i.e. the imaginary part of the permittivity. As a result, the resonance width of the coupled system broadens in addition to the red-shift of the resoance due to the change in ω_p as a function of the incident intensity. A broadened resonace of the coupled system reduces Δn_{max} at on- or near-resonance wavelengths and enhances Δn_{max} at far from resonance. The presence of the antennas thus amplify the change in the refractive index by upto a factor of 20. Moreover, the presence of the antenna introduces an intensity enhancement of at least a factor of ~ 50 at normal incidence (Fig. S4). Thus, even at the saturation intensities these two effects combined can explain a factor of 1000 enhancement of the value of n_2 of the coupled structure compared to that of the the bare ITO at $\lambda = 1400$ nm.

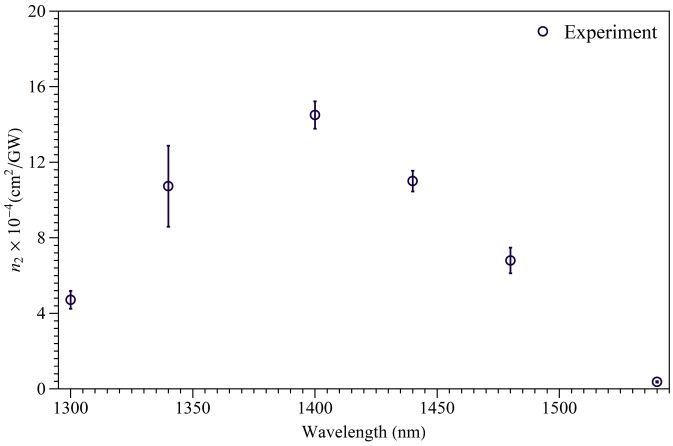

(a)

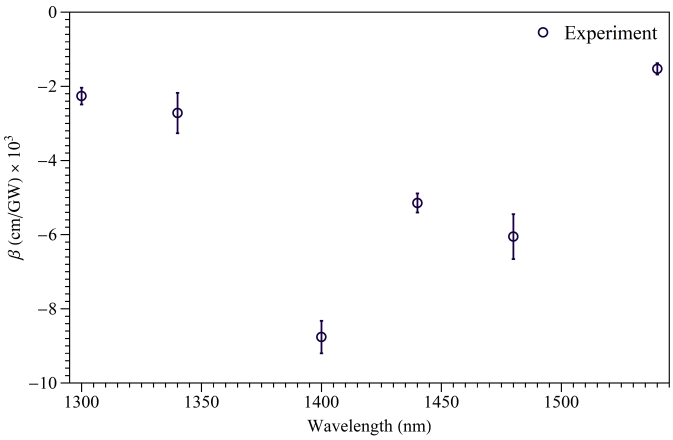

(b)

Figure S6. Measured nonlinear response of low conductivity ITO: (a) The effective nonlinear refractive index n_2 as measured using Z-scan. We use a 23-nm-thick ITO, which is used as the ENZ layer in the coupled structure, for this measurement. (b) The nonlinear absorption coefficient β.

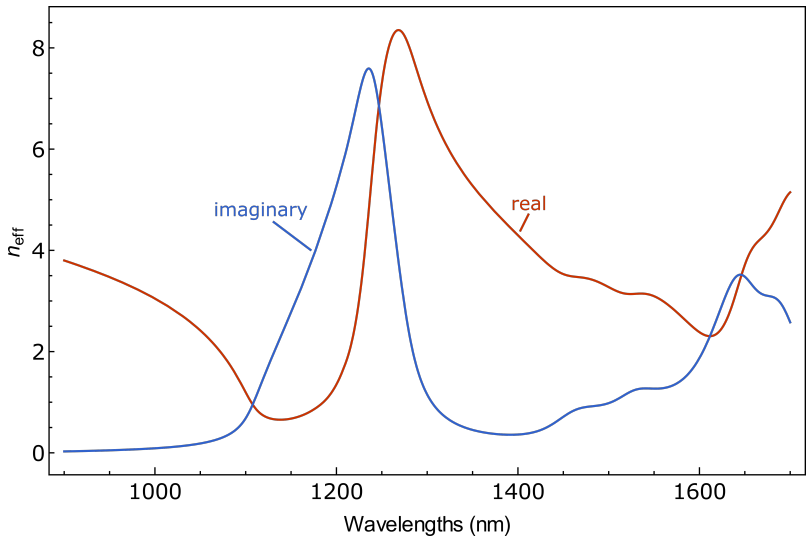

Figure S7. Homogenized refractive index: We used a refractive index homogenization technique to obtain the effective index of the antenna-ITO coupled system. The large effective nonlinear response can understood as the light induced time-dependent shift and reshaping of the homogenized linear dispersion of the coupled system.

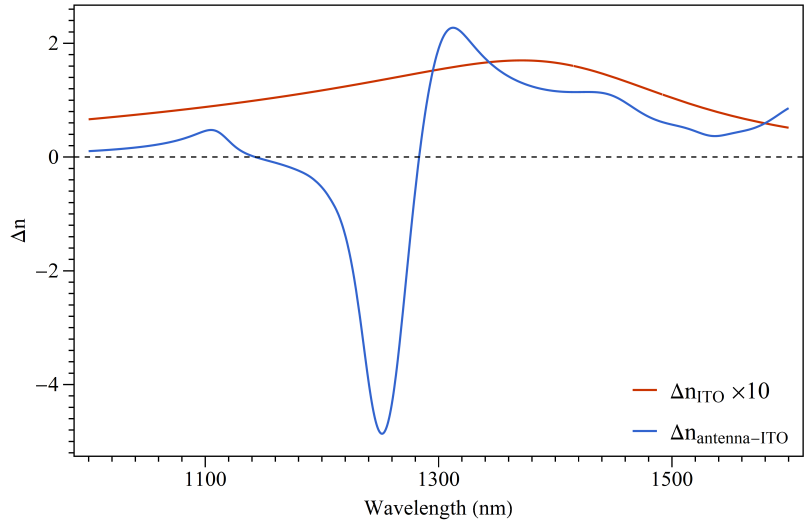

Figure S8. Change in the refractive index due to a red-shift of the plasma frequency: The plot shows that due to the presence of the antenna, a 5% change in the plasma frequency can lead to a much larger change in the refractive index in the coupled structure compared to the bare ITO. Moreover, the required incident intensity to induce a constant amount of red-shift in the plasma frequency is much smaller in the coupled structure than the bare ITO due to the field enhancement. Here, we calculate the change in the refractive index Δn simply by subtracting $\sqrt{\varepsilon(\omega_p)}$ from $\sqrt{\varepsilon(0.95\omega_p)}$. In order to calculate the refractive index for a particular plasma frequency, we use the Lorentz-Drude model and the homogenized refractive index for the bare ITO and the coupled system respectively.

Z-scan traces

We show representative Z-scan traces in the presence of large nonlinear absorption in Fig. S9a ($\lambda = 1340$nm). To obtain the nonlinear measurements, we use a pellicle beam splitter placed right after the sample to divide the beam in order to simulatenously measure closed- and open-aperture signals. We also use a reference photodiode to monitor the power fluctuation. We do two sets of measurements for each wavelength in order to calculate n_2 and β values: one set of measurements with the incident intensity low enough so that nonlinear response is absent; and the other set with an incident intensity large enough ($\sim 150\text{MW}/\text{cm}^2$) to induce a nonlinear response. We normalize the open-aperture signal by dividing the high intensity signal (normalized by the reference signal to account for the power fluctuation) by the low intensity signal (normalized by the reference signal to account for the power fluctuation). In order to find the value of the imaginary part of the phase shift we fit the normalized data to curves generated numerically, as described in the method section. For the closed-aperture signal we find the best fit after dividing the closed-aperture data by the open-aperture data. Finally, we calculate the n_2 and β values from the phase shifts using the standard equations.[20]

We perform a series of measurements with varying intensity to find the maximum possible phase shift – and the change in the refractive index – as shown in Fig. 3. We observed that for a sufficiently large incident intensities the fifth-order nonlinear effects can become important (Fig. S9b). This is the case for some of the data points in Fig. 3. In such cases, we do not divide the closed-aperture signal with the open-aperture signal in order to decouple the nonlinear refraction from the nonlinear absorption. Instead, we find the real part of the nonlinear phase shift by finding the best fit lines while taking the third- and fifth-order nonlinear absorptions into account (Fig. S9b). The phase shifts obtained with such large intensities were used to find the maximum intensity-dependent change in the refractive index (Δn) shown in Fig. 3 of the main text. The values of n_2 and β were obtained using a much lower input intensity, as mentioned above.

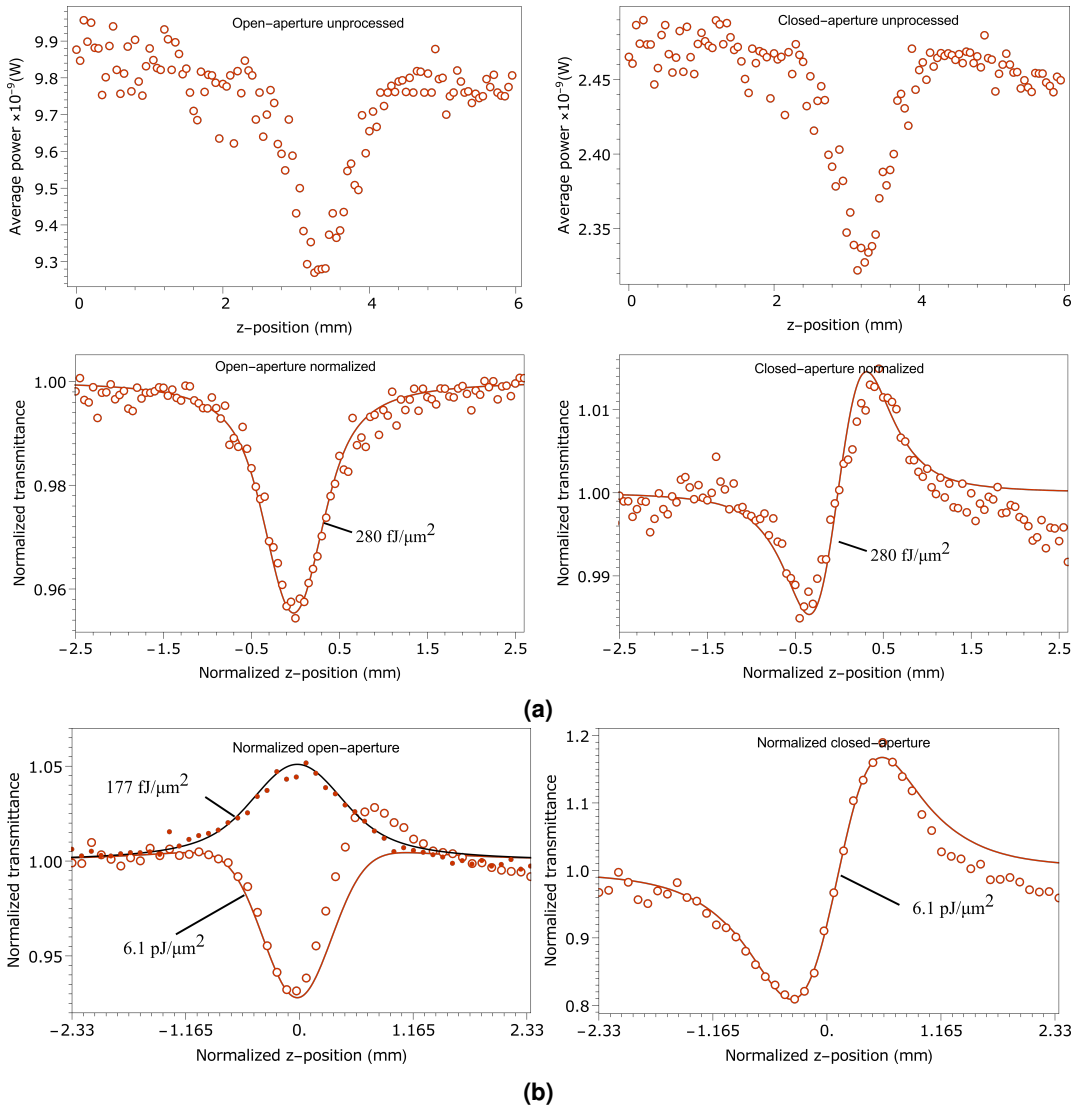

Figure S9. Z-scan traces: (a) Unprocessed (top panel) and processed data (bottom panel) for Z-scan signals at $\lambda = 1340$ nm for incident intensity of ~ 158 MW/cm^2. We obtained the normalized closed-aperture signal after dividing the closed-aperture signal with the open-aperture signal. We obtain the nonlinear phase shifts values - real phase shift = 0.055 rad and imaginary phase shift = 0.043 rad - by fitting the data with the numerically obtained curves (solid lines). (b) Normalized open- and closed-aperture signal at $\lambda = 1440$ nm for real phase shift of ~ 0.57 rad which is equivalent to $\Delta n = 2.61$. In this case, both third- and fifth-order nonlinear absorptions are important. In order to extract the phase shift from the z-scan traces, it is necessary to normalize the signal in such a way so that the transmittance far from focus approaches 1.0.

Reference	$\lvert n_2 \rvert (\text{cm}^2/\text{GW})$	λ(nm)
ITO ($R_s = 70-100\ \Omega/\text{sq.}$)[18]	4.0×10^{-5}	1000
ITO ($R_s = 8-12\ \Omega/\text{sq.}$)[18]	1.6×10^{-3}	1000
Dimer antenna-ITO[18]	5.9×10^{-2}	1000
ITO ($R_s = 4.5\ \Omega/\text{sq.}$)[19]	2.6×10^{-3}	1240
ITO ($R_s = 80\ \Omega/\text{sq.}$) (this work)	1.5×10^{-3}	1400
Dipole antenna-ITO (this work)	3.73	1240

Supplementary Table 1. Comparison of nonlinear response of ITO and hybrid ITO-antenna system at normal incidence.

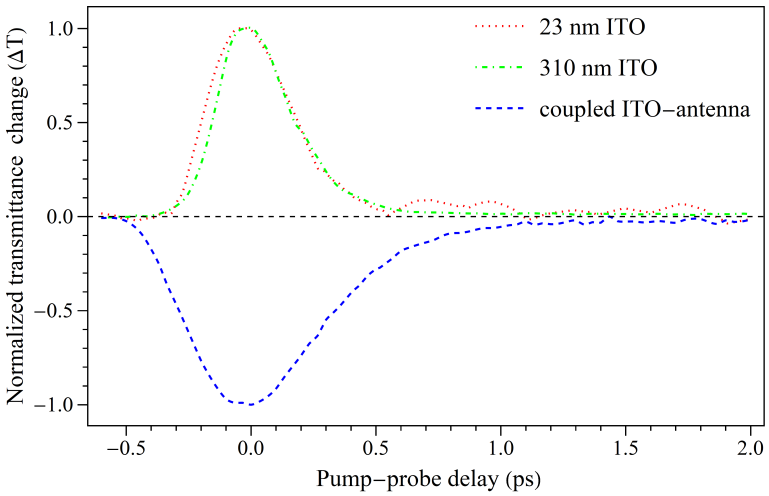

Figure S10. Response time: Normalized pump-probe transmittance of 23 nm thin ITO, 310 nm thick ITO and ITO-antenna coupled system at 1300 nm wavelength. The Pump-probe response time for the coupled system is longer than that of the thin (low conductivity) or thick (high conductivity) ITO films. We normalized the x-axis such that the zero pump-probe delay time corresponds to the maximum transmittance for visual aid.

References

1. Campione, S., Kim, I., de Ceglia, D., Keeler, G. A. & Luk, T. S. Experimental verification of epsilon-near-zero plasmon polariton modes in degenerately doped semiconductor nanolayers. *Optics Express* **24**, 18782–18789 (2016).
2. Campione, S., Brener, I. & Marquier, F. Theory of epsilon-near-zero modes in ultrathin films. *Phys. Rev. B* **91**, 121408 (2015).
3. Schulz, S. A. *et al.* Optical response of dipole antennas on an epsilon-near-zero substrate. *Physical Review A* **93**, 063846 (2016).
4. Campione, S., Wendt, J. R., Keeler, G. A. & Luk, T. S. Near-infrared strong coupling between metamaterials and epsilon-near-zero modes in degenerately doped semiconductor nanolayers. *ACS Photonics* **3**, 293–297 (2016).
5. Vassant, S. *et al.* Epsilon-near-zero mode for active optoelectronic devices. *Physical review letters* **109**, 237401 (2012).
6. Liu, X. *et al.* Quantification and impact of nonparabolicity of the conduction band of indium tin oxide on its plasmonic properties. *Applied Physics Letters* **105**, 181117 (2014).
7. Kane, E. O. Band structure of indium antimonide. *Journal of Physics and Chemistry of Solids* **1**, 249–261 (1957).
8. Chakravarti, A. & Nag, B. Generalized einstein relation for degenerate semiconductors having non-parabolic energy bands. *International Journal of Electronics Theoretical and Experimental* **37**, 281–284 (1974).
9. Guo, P., Schaller, R. D., Ketterson, J. B. & Chang, R. P. H. Ultrafast switching of tunable infrared plasmons in indium tin oxide nanorod arrays with large absolute amplitude. *Nature Photonics* **10**, 267–273 (2016).
10. Guo, P. *et al.* Large optical nonlinearity of ito nanorods for sub-picosecond all-optical modulation of the full-visible spectrum. *Nature Communications* **7**, 12892 (2016).
11. Brorson, S., Fujimoto, J. & Ippen, E. Femtosecond electronic heat-transport dynamics in thin gold films. *Physical Review Letters* **59**, 1962 (1987).
12. Sun, C.-K., Vallee, F., Acioli, L., Ippen, E. & Fujimoto, J. Femtosecond investigation of electron thermalization in gold. *Physical Review B* **48**, 12365 (1993).
13. Carpene, E. Ultrafast laser irradiation of metals: Beyond the two-temperature model. *Physical Review B* **74**, 024301 (2006).
14. Lin, Z., Zhigilei, L. V. & Celli, V. Electron-phonon coupling and electron heat capacity of metals under conditions of strong electron-phonon nonequilibrium. *Physical Review B* **77**, 075133 (2008).
15. Yagi, T. *et al.* Analysis on thermal properties of tin doped indium oxide films by picosecond thermoreflectance measurement. *Journal of Vacuum Science & Technology A* **23**, 1180–1186 (2005).

16. Voisin, C., Fatti, N. D., Christofilos, D. & Vallée, F. Ultrafast electron dynamics and optical nonlinearities in metal nanoparticles. *The Journal of Physical Chemistry B* **105**, 2264–2280 (2001).

17. Smith, D. R., Schultz, S., Markoš, P. & Soukoulis, C. Determination of effective permittivity and permeability of metamaterials from reflection and transmission coefficients. *Physical Review B* **65**, 195104 (2002).

18. Abb, M., Albella, P., Aizpurua, J. & Muskens, O. L. All-optical control of a single plasmonic nanoantenna–ito hybrid. *Nano letters* **11**, 2457–2463 (2011).

19. Alam, M. Z., De Leon, I. & Boyd, R. W. Large optical nonlinearity of indium tin oxide in its epsilon-near-zero region. *Science* **352**, 795–797 (2016).

20. Sheik-Bahae, M., Said, A. A., Wei, T.-H., Hagan, D. J. & Van Stryland, E. W. Sensitive measurement of optical nonlinearities using a single beam. *IEEE Journal of Quantum Electronics* **26**, 760–769 (1990).